

# Probing Langmuir monolayer self-assembly in condensed and collapsed phases: grazing incidence X-ray diffraction and X-ray standing waves studies

K.V. Nikolaev<sup>1,2</sup>, L.R. Muftakhova<sup>1,2</sup>, G.M. Kuz'micheva<sup>3</sup>, Yu.N. Malakhova<sup>2</sup>,  
A.V. Rogachev<sup>2</sup>, N.N. Novikova<sup>2</sup>, and S.N. Yakunin<sup>2</sup>

<sup>1</sup>Moscow Institute of Physics and Technology, Dolgoprudny, Russia

<sup>2</sup>National Research Center Kurchatov Institute, Moscow, Russia

<sup>3</sup>MIREA – Russian Technological University, Moscow, Russia

November 20, 2024

## Abstract

Ce-induced effects on the self-assembly of arachidic acid Langmuir monolayers was studied in this work. The monolayers were formed on the liquid subphase in the presence of Ce(III) ions. A new type of structural configuration is found for such monolayers, in which the monolayer maintains its structural ordering despite being compressed beyond the collapse point. Instead of forming 3D aggregates as in the typical collapsed state, the monolayer appears to be corrugated. Grazing incidence X-ray diffraction and X-ray standing waves confirm these findings. The diffraction pattern for the monolayer in a new state is represented by the unclosed diffraction rings with maxima near the sample horizon. This diffraction pattern is quantitatively reproduced in the numerical simulations by assuming the corrugated monolayer. The details of the conditions under which these corrugated Langmuir monolayers were observed and the analysis of the diffraction data are described.

## 1 Introduction

Scientific interest in the self-assembly of amphiphilic trivalent lanthanide complexes is motivated by their photophysical properties, which can be exploited for molecular sensing [1]. The practical realization of such systems requires the assembly of the lanthanide complexes into nanostructures [2]. One of the possible ways to create functional nanomaterials with predefined molecular architecture is the Langmuir-Blodgett technique [3], which involves the self-assembly of amphiphiles at the air-liquid interface into a Langmuir monolayer and subsequent transfer to a solid substrate. Charged headgroups of amphiphilic molecules are known to interact with metal ions when present in the liquid subphase [4]. In this way, self-assembly defines the performance of a nanodevice. Self-assembly is driven not only by the sort of amphiphiles and the thermodynamic conditions under which the monolayer is formed [5], but can also be directed by interactions with ions in the subphase [6]. Therefore, further development of such functional devices requires extensive and detailed studies of the structural organization of amphiphilic trivalent lanthanide complexes.

There are two known scenarios of how the interaction with metal ions affects the structure of the Langmuir monolayer, as reported in [7] using divalent metal ions as an example. The first, more common scenario is that the interaction between headgroups and metal ions leads to the formation of a disordered thin monolayer of metal ions underneath the organic monolayer, which affects the compressibility of the monolayer, resulting in structures similar to high-pressure solid-phase monolayers [7]. The second scenario is the formation of the ionic monolayer ordered into a superstructure commensurate with the organic monolayer, which was first reported in [8]. The study reports the formation of a  $\text{Cd}^{2+}$  superstructure underneath an arachidic acid monolayer. The structure has a  $2 \times 3$  cell commensurate with the organic monolayer structure. The transition between these two scenarios of interaction of the organic monolayer with metal ions may depend on the pH of the subphase and the ion concentration. In [9], the interaction of behenic acid with a variety of divalent ions was studied,

and an ion concentration threshold was observed. Above this threshold, the ions formed a superlattice, and the ion layer was disordered below it. Later studies [10, 11] report on forming ordered monolayers of lanthanide ions. They tested a wide range of trivalent lanthanides. They found that the ordering depends not only on the molecules forming the Langmuir monolayer, but also on the atomic number of a lanthanide. In addition, the crystalline structure of the ionic monolayer can be commensurate or incommensurate with the lattice of the organic molecules.

Another interesting aspect is the collapse of Langmuir monolayers in the presence of metal ions. The study in [12] reports the spontaneous collapse of fatty acid monolayers in the presence of  $\text{Ca}^{2+}$  ions. It has also been shown both experimentally [13] and theoretically [14] that the presence of  $\text{Ca}^{2+}$  ions changes the structure of the collapsed fatty acid monolayer. Even more interesting is that the collapsed structures show a high degree of order, namely the formation of inverted bi-layers. The formation of such inverted bi-layers is also reported for lanthanides [15]. Yet again, the structure of the collapsed layers is ion-specific.

Thus, the interaction of fatty acids with lanthanide ions has shown complex and widely varying results. However, understanding the mechanisms of ion monolayer formation and its effect on collapse is relevant to the problems of functionalizing lanthanides into self-assembled nanostructures. This article focuses on the self-assembly of arachidic acid monolayers in the presence of  $\text{Ce}^{3+}$  ions and their structural reorganization while compressed beyond the collapse point. We have studied the structure of fatty acid monolayers interacting with metal ions at the air-liquid interface at different surface pressures and temperatures. As the primary tool for monitoring the monolayer structure, we used grazing incidence X-ray diffraction (GID) at the bending magnet synchrotron radiation source. This choice is due to the sensitivity of GID to both translational and orientational lateral ordering of the monolayers. In addition, simultaneously with GID experiments, we performed the X-ray standing wave (XSW) measurements to monitor the vertical localization of  $\text{Ce}^{3+}$  ions during the structural reorganization at the collapse.

## 2 Results

### 2.1 Surface pressure-area isotherms

The effect of  $\text{Ce}^{3+}$  ions on the thermodynamic properties of the arachidic acid monolayer was investigated in our additional series of experiments using compression isotherm measurements. We have studied the behavior of the arachidic acid monolayer, formed on  $\text{Ce}^{3+}$  solution and on pure water as a control. All measurements were performed at a temperature of  $T = 21^\circ\text{C}$ . The typical  $\pi$ - $A$  isotherms are shown in Fig. 1. Based on these experimental results, the key feature of the arachidic acid monolayer formed in the presence of  $\text{Ce}^{3+}$  is the absence of a liquid phase, as evidenced by a high monolayer compressibility – 2.2 m/mN.

Our observations are consistent with the results reported in [16], where detailed studies of the binding interaction of lanthanide ions ( $\text{La}^{3+}$  and  $\text{Y}^{3+}$ ) with arachidic acid monolayers at submicromolar salt concentrations were reported. Note that similar changes in the isotherms were observed in [17], where the effect of  $\text{Cu}^{2+}$  on the organization and morphology of the arachidic acid monolayer was studied.

Generally, metal binding with carboxylate acid groups is recognized to promote the formation of a rigid monolayer with higher crystallinity and reduced molecular area [18]. The interaction of divalent and trivalent

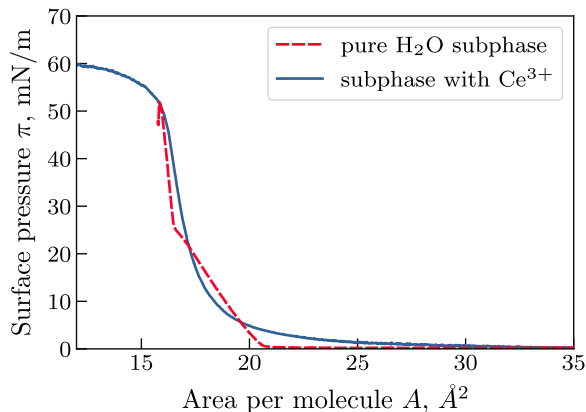


Figure 1: Surface pressure  $\pi$  - area  $A$  isotherms measured for the arachidic acid monolayer deposited on pure water (red line) and on water with  $\text{Ce}^{3+}$  ionic solution (blue line). The isotherm measured on pure water corresponds to a compression with two phase transitions: condensation and solidification. The isotherm measured for a monolayer on a subphase containing  $\text{Ce}^{3+}$  ions is characteristic of a phase transition from gas to solid with a compressibility of 2.2 m/mN, bypassing the liquid phase.

metallic ions with carboxylic groups of fatty acids is strongly dependent on such parameters as solution pH, temperature, salt concentration. The type of metal-carboxylate complex (ionic, unidentate, chelating bridging bidentate, polymeric tridentate) is determined to a large extent by metallic ion specific nature, i.e. ion size, coordination structure, oxidation state in solution, etc. Large  $\text{Ln}^{3+}$  ions with high coordination numbers exhibit rather intricate binding behavior [16], resulting in a wide variety of the lanthanide-carboxylate binding interactions. According to the data reported in [16], at least three different coordination modes for carboxylate headgroups with lanthanide cations ( $\text{La}^{3+}$  and  $\text{Y}^{3+}$ ) have been identified at the air/water interface. Furthermore, the relative ratio between the different complexes was found to depend on the salt concentration in the subphase. Thus, the intricacies of the lanthanide complexation behavior impose structural complications on the self-assembly processes in the fatty acid monolayers. The underlying mechanisms regulating these processes are the main focus of our studies.

## 2.2 Brewster angle microscopy

We performed BAM measurements of the arachidic acid monolayer formed on  $\text{Ce}^{3+}$  solution to visualize the changes in morphological properties at different monolayer phases. The representative BAM images are shown in Fig. 2. As can be seen, the BAM data obtained for the gas and solid phases indicate the formation of a uniform sheet-like layer. This kind of BAM images are usually recorded for fatty acid formed on a subphase with metal ions [17].

Effects in the phase behavior of the arachidic acid monolayer induced by Ce were observed in BAM measurements in the collapse region (see Fig. 2). We performed BAM studies of the arachidic acid monolayer at two different temperatures,  $T = 21^\circ\text{C}$  and  $T = 23^\circ\text{C}$ . BAM images taken at  $T = 23^\circ\text{C}$  showed the formation of large 3D crystalline-like aggregates. Such disordered structures are often observed in BAM studies of the collapse behavior of fatty acid monolayers. In contrast, the post-collapse BAM data obtained for the low temperature monolayer ( $T = 21^\circ\text{C}$ ) revealed the mosaic-like texture of the monolayer. As shown in Figs. 2(e), 2(f), the

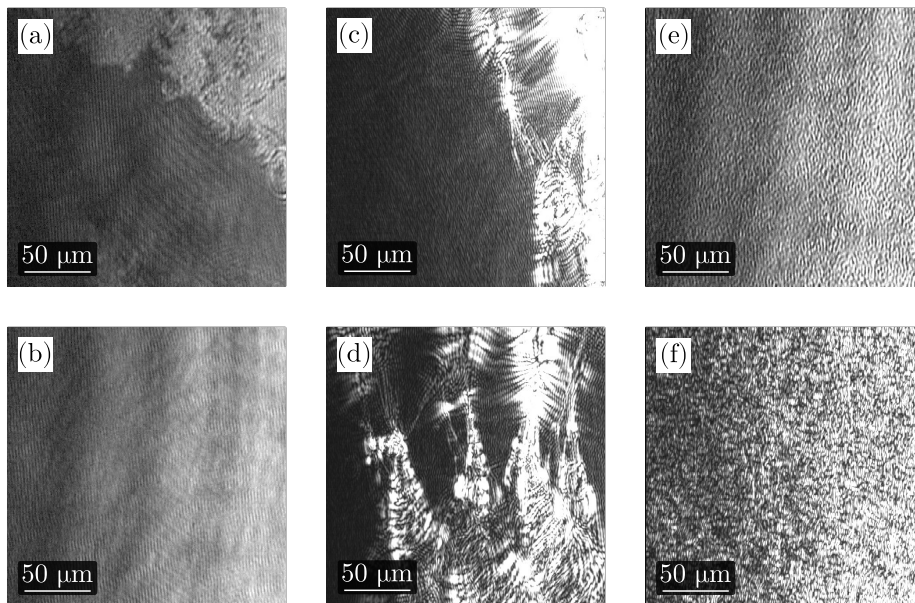


Figure 2: Brewster angle microscopy images of arachidic acid monolayers formed on the aqueous solution of the  $\text{Ce}(\text{NO}_3)_3 \cdot 6\text{H}_2\text{O}$  salt. The images were taken at different stages of compression: (a)  $\pi = 0.4$  mN/m; (b)  $\pi = 35$  mN/m; (c)  $\pi = 57$  mN/m; (d)  $\pi = 58$  mN/m. The growth of the large crystalline-like aggregates can be seen in images (c) and (d) taken beyond the collapse point. The images (a)–(d) were taken at the temperature  $T = 23^\circ\text{C}$ . The appearance of the mosaic-like collapse structure at the lower temperature  $T = 21^\circ\text{C}$  is shown in (e) and (f). The image (e) was taken just beyond the collapse point, the image (f) was taken when the monolayer was further compressed.

	range A				range B		range C			
	$(0\ 1/2)$		$(1/3\ 1/2)$		$(2/3\ 0)$		$(11), (1\bar{1})$		$(0\ 2)$	
	$Q_{\parallel}, \text{\AA}^{-1}$	$\delta, \text{\AA}^{-1}$	$Q_{\parallel}, \text{\AA}^{-1}$	$\delta, \text{\AA}^{-1}$	$Q_{\parallel}, \text{\AA}^{-1}$	$\delta, \text{\AA}^{-1}$	$Q_{\parallel}, \text{\AA}^{-1}$	$\delta, \text{\AA}^{-1}$	$Q_{\parallel}, \text{\AA}^{-1}$	$\delta, \text{\AA}^{-1}$
<b>control</b>	—	—	—	—	—	—	1.496	0.03	1.496	0.04
<b>series 1</b>	0.371	0.01	0.581	0.02	—	—	1.491	0.03	1.548	0.02
<b>series 2*</b>	0.379	0.01	0.583	0.02	—	—	1.499	0.02	1.555	0.03
	—	—	—	—	0.961	0.02	1.6 <sup>(11)</sup> 1.637 <sup>(1<math>\bar{1}</math>)</sup>	0.07 <sup>(11)</sup> 0.01 <sup>(1<math>\bar{1}</math>)</sup>	1.479	0.01
<b>series 3</b>	0.376	0.02	**	**	—	—	1.491	0.01	1.547	0.02
<b>series 4</b>	—	—	—	—	0.959	0.02	1.595 <sup>(11)</sup> 1.633 <sup>(1<math>\bar{1}</math>)</sup>	0.02 <sup>(11)</sup> 0.03 <sup>(1<math>\bar{1}</math>)</sup>	1.476	0.02

Table 1: Table of peak coordinates  $Q_{\parallel}$  and corresponding full width at half maximum delta. The peaks are grouped by their  $Q_{\parallel}$  in three ranges: range A:  $Q_{\parallel} \sim [0.3, 0.6] \text{\AA}^{-1}$ , range B:  $Q_{\parallel} \sim 0.9 \text{\AA}^{-1}$  and range C:  $Q_{\parallel} \sim [1.4, 1.7] \text{\AA}^{-1}$ . \*) The peaks of series 2 are assigned to the two coexisting phase modes, so this series is split into two rows in the table. \*\*) Peak  $(1/3\ 1/2)$  was not measured, but can be assumed to exist because  $(0\ 1/2)$  was measured and by analogy with series 1 and 2. These estimates are made by fitting the Gaussian profile to the data. For brevity, the uncertainties of these estimates are omitted. The values are given in the order of magnitude of the uncertainties. These uncertainties are further used to calculate the crystal structure errors in Table 2.

monolayer surface is divided into many two-dimensional patches, which can be identified as anisotropic domains that appear homogeneously across the monolayer upon compression. It should be emphasized that no growth of these domains into crystalline-like aggregates was observed upon further compression of the monolayer. In addition, BAM images taken at  $T = 21^{\circ}\text{C}$  near the collapse pressure revealed another interesting feature of the deformation processes in the collapse. As can be seen in Fig. 2(e), the surface of the monolayer is weakly grooved in the direction parallel to the barrier, which is a clear indication of the preferred deformation direction at the beginning of the collapse.

Taken together, the presented BAM studies of arachidic acid monolayers formed on a subphase containing  $\text{Ce}^{3+}$ , revealed differences in the morphological properties of two observed collapsed modes. Thus, in our further discussion, the collapse with disordered morphology will be referred to as *collapse mode 1*; whereas the collapse with specific mosaic-like morphology will be referred to as *collapse mode 2*.

Note that similar results are reported in [19], where two qualitatively different collapse morphologies are also observed in fatty acid monolayers. They used phase contrast microscopy to study the collapse processes in the stearic acid monolayer as a function of the pH of the water subphase. According to the experimental data [19], the occurrence of collapse structures seen as bright random cracks was detected at  $\text{pH} = 7.8$ , while a surface roughening collapse pattern was observed at  $\text{pH} = 7.5$ .

## 2.3 Grazing incidence diffraction

Five series of GID measurements were performed in our studies. Each series was designed to study the structure of the arachidic acid monolayer at a different combination of surface pressure and temperature. There is one control series in which the arachidic acid monolayers were deposited on pure water subphase and four series in which arachidic acid monolayers were formed on a 20 mM  $\text{Ce}(\text{NO}_3)_3 \cdot 6\text{H}_2\text{O}$  salt solution. Other series were designed to study the solid state and the post-collapse state of the monolayer in the presence of  $\text{Ce}^{3+}$  ions in the liquid subphase. Within each series, except the control, multiple samples of the monolayer were prepared and measured. This was done to ensure reproducibility. The monolayers were compressed to a specified surface pressure at a specified temperature chosen for each series. The results are shown in Fig. 3. The measurements from the most representative samples are selected to be shown. From these selected samples, all collected data were integrated into a single GID pattern to represent each series. Some measurements were taken with different



	Organic lattice				HC chain ordering		Super structure	
	$a$ , Å	$b$ , Å	$\gamma$ , deg	A, Å <sup>2</sup> p.m.	tilt	packing	inorganic	organic
<b>control</b>	$4.85 \pm 0.02$	$8.40 \pm 0.02$	90	$20.4 \pm 0.1$	NN	—	—	—
<b>series 1</b>	$4.93 \pm 0.03$	$8.12 \pm 0.02$	90	$20.0 \pm 0.2$	NN	—	$3 \times 2$	—
<b>series 2</b>	$4.90 \pm 0.03$	$8.12 \pm 0.02$	90	$19.8 \pm 0.2$	NN	—	$3 \times 2$	—
	$4.4 \pm 0.2$	$8.5 \pm 0.1$	$88 \pm 5$	$19 \pm 1$	no tilt	PHB	—	$3 \times 1$
<b>series 3</b>	$4.93 \pm 0.02$	$8.12 \pm 0.02$	90	$20.0 \pm 0.1$	NN	—	$3 \times 2$	—
<b>series 4</b>	$4.38 \pm 0.02$	$8.52 \pm 0.02$	$88.3 \pm 0.4$	$18.6 \pm 0.1$	no tilt	PHB	—	$3 \times 1$

Table 2: List of lattice parameters (rectangular centered cell assumed), phase modes corresponding to the orientational ordering of the hydrocarbon chains and superstructures as deduced from the GID patterns in Fig. 3.

resolution or different scan area. These measurements are superimposed on the GID pattern, which is indicated by vertical dashed lines. It is important to note that for some measurements the GID pattern has evolved over time. Since the data is integrated over all measurements, different stages of structural change are captured as "motion blur" in Fig. 3. For such cases, the time evolution is shown in Figs. 4, 5 and 6.

We group the observed diffraction peaks into three ranges according to their  $Q_{\parallel}$  coordinate. Range A: low spatial frequency  $Q_{\parallel} \sim [0.3, 0.6] \text{ \AA}^{-1}$ . Range B: medium spatial frequency  $Q_{\parallel} \sim 0.9 \text{ \AA}^{-1}$ . Range C: high spatial frequency  $Q_{\parallel} \sim [1.4, 1.7] \text{ \AA}^{-1}$ ; this is the range in which a typical diffraction pattern from a Langmuir monolayer is observed. The peak coordinates and corresponding full width at half maximums are listed in Table 1. Finally, the crystal structure is inferred from the GID patterns for each series. The results are shown in Table 2. Note that throughout this article we use the rectangular centered unit cell with the corresponding peak index notation.

### Control series: monolayer on pure water

An arachidic acid monolayer was formed on the surface of pure water and compressed to a surface pressure  $\pi = 20 \text{ mN/m}$  at temperature  $T = 21^{\circ}\text{C}$ . In this series of measurements [see Fig. 3(a)] a typical GID pattern for a Langmuir monolayer was observed: a triplet of peaks (02), (11), and ( $1\bar{1}$ ). The brighter peak at the horizon of the monolayer is the (02) peak, the peak above the horizon is a degenerate peak, in which two peaks (11) and ( $1\bar{1}$ ) are superimposed. The arrangement of the peaks on top of each other indicates a hexagonal lattice:  $b = \sqrt{3}a$ ,  $\gamma = 90^{\circ}$ . The tails of the fatty molecules are inclined with respect to the surface and are tilted in the direction of the nearest neighbor which corresponds to the NN tilt phase mode. We infer this from the arrangement of peaks (02) on the horizon and (11) directly above, which is characteristic of the NN tilt [5].

### Series 1: solid-phase monolayer at $T = 23^{\circ}\text{C}$

The monolayer has been compressed to a surface pressure  $\pi = 20 \text{ mN/m}$  at  $T = 23^{\circ}\text{C}$ . GID data were collected continuously over a 13 hour period in multiple exposures. The integrated GID pattern is shown in Fig. 3(b). The surface pressure was kept constant at  $\pi = 20 \text{ mN/m}$  throughout all exposures. The GID patterns in all exposures are equivalent down to the measurement noise. Thus, the structure is unchanged throughout the 13 hour period. This is quite remarkable because it indicates that the monolayer was not damaged by the radiation. Note that the radiation damage is a typical problem in the synchrotron studies of Langmuir monolayers, see e.g. [20]. Here, we would like to highlight the importance of measuring the GID at lower intensities and with longer exposures, as the self-assembly process may be slower than the degradation induced by radiation. From this point of view, measuring on a bending magnet beamline can be advantageous compared to brighter sources such as insertion devices.

In addition to a conventional GID pattern for a fatty acid monolayers in range C, we observed additional peaks in range A in this series. In range C we again see a (02) peak at the horizon and a degenerated peak

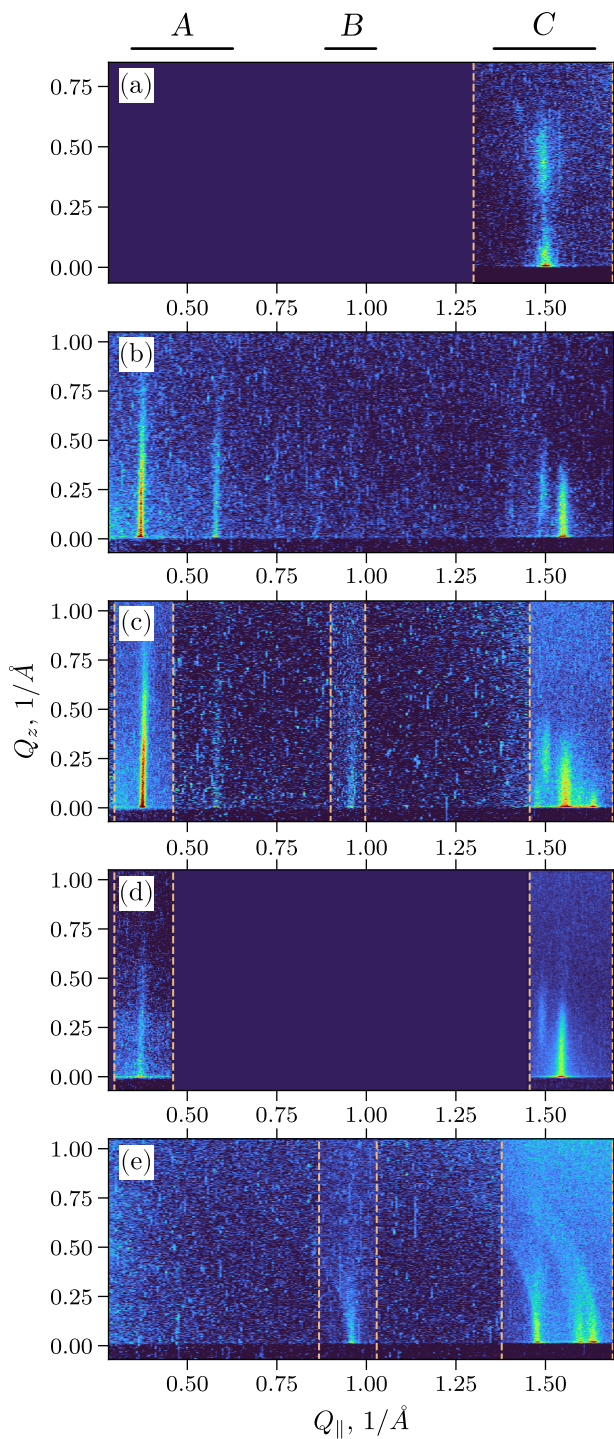


Figure 3: Summary of all GID pattern measurements. (a) control series (b) – (e) series 1 through 4, respectively. Each pattern is collected from all measurements made on a selected, most representative sample in the series. Some measurements are taken in the different  $Q_{\parallel}$  range. This is indicated by the vertical dashed lines. The diffraction peaks are grouped by their  $Q_{\parallel}$  coordinate into three ranges: A, B and C.

(11),  $(1\bar{1})$  above the horizon. However, the GID pattern observed in the control series, the (02) peak is shifted horizontally to higher frequencies. This implies a lattice with tighter packing, compared to that of the arachidic monolayer on pure water: the surface area occupied by a molecule is reduced;  $20 \text{ \AA}^2$  for series 1 versus  $20.4 \text{ \AA}^2$  for control. The lattice is not hexagonal ( $b \neq \sqrt{3}a$ ), however the lattice angle is the same:  $\gamma = 90^\circ$ . The structure has NN tilt.

Of particular interest are the bright peaks in the range A. We attribute these peaks to diffraction at a layer formed by  $\text{Ce}^{3+}$  ions adsorbed at the bottom of the monolayer on the surface of the subphase. This assumption is confirmed by two observations. First, the low spatial frequencies  $Q_{\parallel}$  of the peaks imply a larger spatial period compared to the organic lattice. The  $Q_{\parallel}$  coordinates of these peaks correspond to the fractional

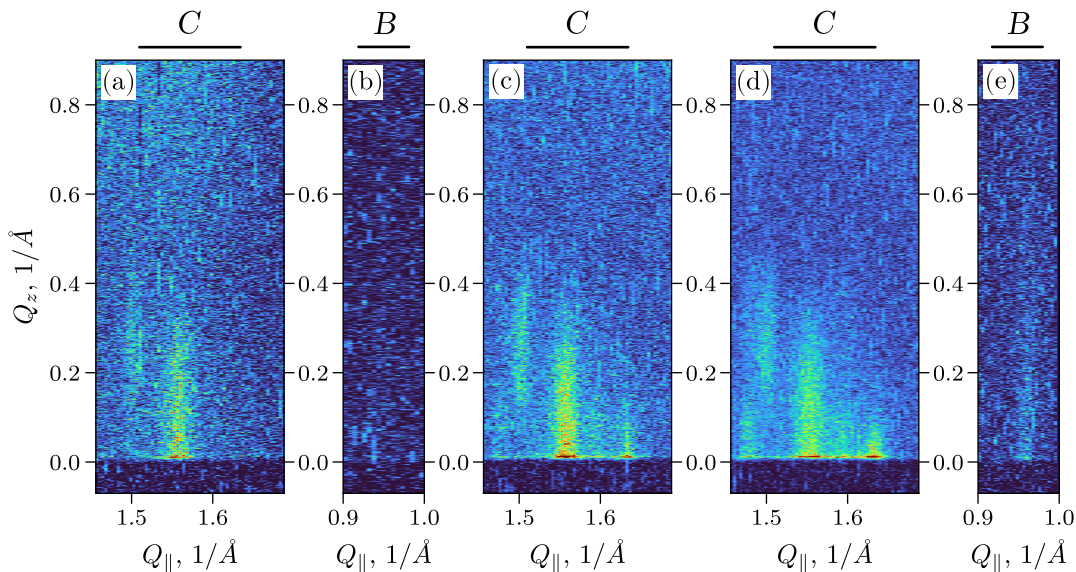


Figure 4: Time evolution of the GID pattern in series 2. The start and end times of the measurement in terms of hours elapsed after monolayer compression: (a) 2 – 3 hrs. (b) 3 – 7 hrs. (c) 7 – 11 hrs. (d) 11 – 18 hrs. (e) 21 – 22 hrs. Patterns are measured in different  $Q_{\parallel}$  ranges, which are indicated above the frames. Such a change in the GID pattern indicates that the monolayer was initially in a solid phase with an NN tilt and an inorganic superstructure, after which there was a coexistence of solid phase modes with an NN tilt and a PHB ordering.

indices  $(0\frac{1}{2})$  and  $(\frac{1}{3}\frac{1}{2})$  of the reciprocal unit cell of the arachidic acid monolayer. This implies that  $\text{Ce}^{3+}$  ions form a superstructure underneath the arachidic acid monolayer. The unit cell of such a superstructure has a size of  $3 \times 2$  unit cells of the arachidic acid lattice. Second, the vertical size of the inorganic lattice peaks at  $(Q_{z,\text{max}} \sim 0.8 \text{ \AA}^{-1})$  is significantly larger than that of the organic lattice peaks  $(Q_{z,\text{max}} \sim 0.4 \text{ \AA}^{-1})$ , indicating a greater vertical spatial localization of  $\text{Ce}^{3+}$  ions compared to that of the arachidic acid molecules. The formation of the  $\text{Ce}^{3+}$  layer at the subphase interface below the monolayer is also supported by the XSW measurements, as will be discussed in the next section. We will refer to the superstructure of  $\text{Ce}^{3+}$  ions as the *inorganic superstructure*.

### Series 2: solid-phase monolayer at $T = 21^\circ\text{C}$

The monolayer was compressed to a surface pressure of  $\pi = 20 \text{ mN/m}$  as in series 1. However, this time the samples was prepared at a lower temperature of  $T = 21^\circ\text{C}$ . All GID measurements from a selected sample are integrated and shown in Fig. 3(c). The total duration of the measurements on this sample was 22 hours. The surface pressure was kept constant throughout the measurements.

The GID pattern changed during the measurements, its evolution is shown in Fig. 4. Similar to series 1, it exhibits a typical GID pattern, characteristic of an NN tilt, in the range C [see Fig. 4(a)]. This pattern was first observed 3 hours after compression. The full range measurement shown in Fig. 3(c) was performed over the next 4 hours. A part of this measurement is also shown in Fig. 4(b) to emphasize that no peaks were detected in the B region during this period. The GID pattern of the inorganic superstructure was also observed [see peaks in range A in Fig. 3(c)]. The change in GID pattern was first observed 11 hours after compression [see Fig. 4(c)]. It evolved to a final GID pattern [see Fig. 4(d)] during another 7 hours of measurements. In this pattern we observed five peaks in the range C. Three more peaks appear in addition to the NN pattern. We interpret the pattern in Fig. 4(d) as diffraction from two coexisting packing modes. The additional peaks are an another triplet of  $(11)$ ,  $(1\bar{1})$  and  $(02)$ , corresponding to a new packing mode. Since we can distinguish all three peaks at different  $Q_{\parallel}$ , the lattice in this mode should have an oblique unit cell. We can also conclude that there is no tilt of the arachidic acid molecules, since all three peaks are on the horizon of the sample.

Finally, 22 hours after the compression, we detected another peak at  $Q_{\parallel} = 0.961 \text{ \AA}^{-1}$  in range B. We ascribe this peak with diffraction on a superstructure corresponding to the lattice of a new packing mode. The peak

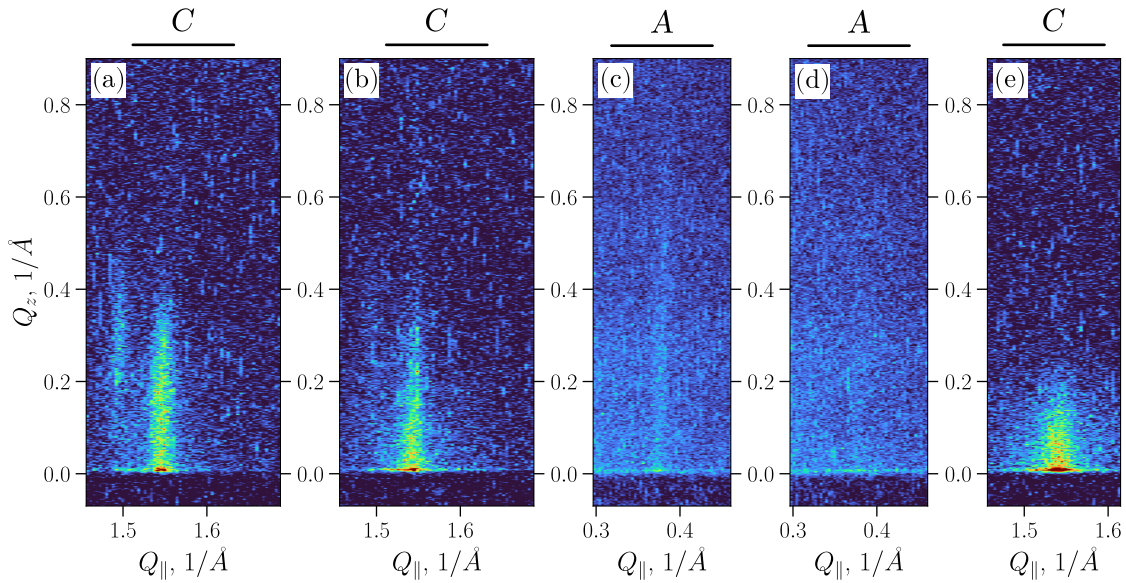


Figure 5: Time evolution of the GID pattern in series 3. The start and end times of the measurement in terms of hours elapsed after monolayer compression: (a) 1 – 2 hrs. (b) 18 – 19 hrs. (c) 21 – 24 hrs. (d) 26 – 29 hrs. (e) 40 – 41 hrs. Patterns are measured in different  $Q_{\parallel}$  ranges, which are indicated above the frames. This evolution of the GID pattern corresponds to the gradual collapse of the monolayer starting from a structure with NN tilt phase and inorganic superlattice to a system with only short range order and no superstructure.

is identified by the fractional indices  $(2/30)$ . In contrast to the diffraction on the inorganic superstructure, this peak is considerably smaller in the  $Q_z$  direction with  $Q_{z,\max} \sim 0.4 \text{ \AA}^{-1}$ . On the other hand, it is comparable in  $Q_{z,\max}$  to the peaks of the organic structure in range C. Therefore, this is not a diffraction at the  $\text{Ce}^{3+}$  lattice, but diffraction on a superstructure composed of the arachidic acid molecules – *organic superstructure*. It can appear in the Langmuir monolayers due to the azimuthal ordering of the hydrocarbon chains of the molecules [21, 22]. Molecules of the monolayer can assume a denser packing due to a specific mutual orientation of the hydrocarbon chains of neighboring molecules, that is called herringbone (HB) an ordering when the azimuth angle between the hydrocarbon chains is  $90^\circ$ , and pseudoherringbone (PHB) ordering when this angle is about  $40^\circ$  [23]. Similar organic superstructure peaks in the GID have also been reported in arachidic acid films in [24], but there the Langmuir-Blodgett multilayers on solid substrate were studied, not the monolayer on liquid. They report a superstructure with  $5 \times 1$  cell and an HB arrangement. The  $(2/30)$  peak in our study can be ascribed to a  $3 \times 1$  superstructure and a PHB arrangement.

To summarize the series 2, the monolayer was initially observed in a solid state phase with rectangular lattice, NN tilt and inorganic superstructure, identical to series 1. However, in contrast to series 1, a new packing mode was observed 11 hours after compression. We attribute this to the PHB ordering. This packing mode coexists with an initial phase.

### Series 3: collapse mode 1

The monolayer samples in this series have been compressed beyond the collapse point. An integrated GID pattern is shown in Fig. 3(d). GID measurements for this sample were taken over a 41-hour period. The working temperature is  $T = 23^\circ\text{C}$ . The surface pressure of 52 mN/m was reached during compression, after which the surface area was kept constant throughout the measurements.

In the first GID pattern measured after compression, we again see a GID pattern characteristic of the NN tilt mode [see Fig. 5(a)]. The GID pattern of the inorganic superstructure was also detected after compression, as seen in the integrated pattern in Fig. 3(d): note the peak in the range A. However, the GID pattern has started to degrade, as shown in Fig. 5(b) measured 19 hours after compression. In addition, the peak from the inorganic superstructure is still visible 24 hours after compression. In the measurement 5 hours later, the peak from the inorganic superstructure has disappeared. Subsequently, the GID pattern of the monolayer in



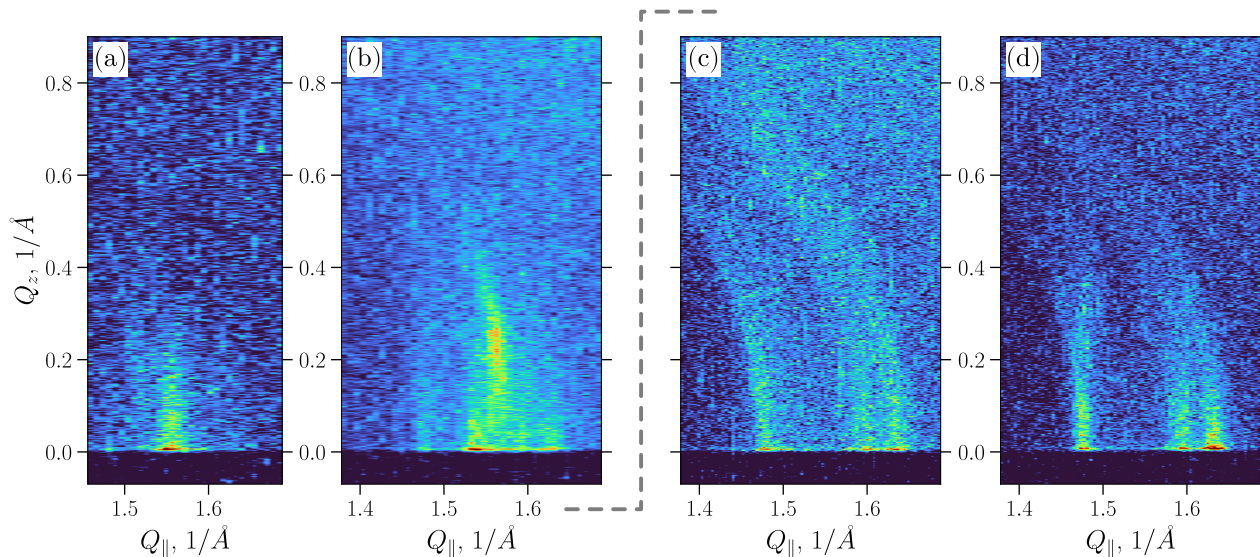


Figure 6: The time evolution of the GID pattern in series 4. Note that the data were measured from two different monolayer samples deposited under the same conditions. (a), (b) is for the first sample, (c), (d) is for the second one. This is indicated by the dashed line. The start and end times of the measurement in terms of hours elapsed after monolayer compression: (a) 0–2 hrs. (b) 3–11 hrs. (c) 3–5 hrs. (d) 22–24 hrs.

the range C also degraded, as shown in Fig. 5(e).

For the inorganic superstructure, only the  $(0\ 1/2)$  peak was followed to save measurement time for resolving the structural change of the monolayer. However, it can be argued that  $(1/3\ 1/2)$  should exist. Indeed, in this series the patterns characteristic of the NN tilt mode and the inorganic structure are detected, as in series 1 and at the beginning of series 2. Since it is attributed to an inorganic superstructure, the  $(1/3\ 1/2)$  is also very likely to exist.

Thus, in series 3, the monolayer was compressed past the collapse point. Initially, the structure of the monolayer was similar to that of a solid phase monolayer as in series 1 and 2, but the structure began to degrade, and 41 hours after compression, only the peak corresponding to the short-range order was present, indicating the lateral disarrangement of the monolayer. The inorganic superstructure has also degraded as a result of the collapse.

#### Series 4: collapse mode 2

In this series, a new collapse mode of the arachidic acid monolayer was studied. The integrated GID pattern is shown in Fig. 3(e). The monolayer has been compressed beyond the collapse point at  $\pi = 52$  mN/m, after which the compression was stopped. The monolayer is studied at temperature  $T = 21^\circ\text{C}$ .

The GID pattern in Fig. 3(e) is unusual for diffraction on a 2D polycrystalline system: the Bragg rods are rounded. The rounding of the peaks is exactly on the circle in reciprocal space and around its origin. In this sense, these peaks are similar to the Scherrer rings characteristic of diffraction on a 3D polycrystalline material. In our case, these diffraction rings are not closed. One can see the rounded rods instead. This suggests that collapse mode 2 is an intermediate state of the monolayer between a 3D and a 2D powder. In fact, the Langmuir film is still in a monolayer state because we still observe the GID pattern characteristic of a monolayer, namely a monolayer with PHB hydrocarbon chain ordering. Moreover, the positions of peaks  $(11)$ ,  $(1\bar{1})$  and  $(02)$  are the same as in series 2 [see Figs. 3(c), 3(e) and Table 1]. Their  $Q_{\parallel}$  coordinates are within 1% deviation between series 2 and 4. There is also a peak in range B [see Fig. 3(e)], again suggesting the PHB phase mode. However, these 2D domains are oriented in 3D with their normal deviating from the normal of the subphase. Presumably, in the collapse mode 2, the structure can be ascribed to a corrugated monolayer, as the domains are randomly oriented with a preferential orientation in the subphase plane.

The time evolution of the monolayer in the collapse mode 2 is shown in Fig. 6. In this series of measurements,

the monolayers underwent a rapid structural change compared to the measurement timescale. We measured both XSW and GID. To do this, we prepared several monolayer samples in collapse mode 2. In Fig. 6 we show GID data from two different samples. For both samples all controllable conditions were the same. On the first sample, we performed the GID measurements immediately after compression. The GID pattern measured within the first 2 hours is shown in Fig. 6(a), and the data collected between 3 and 11 hours after compression are shown in Fig. 6(b). On the second sample, we first performed the XSW measurements, which will be discussed in the next section, starting at 3 hours after compression we performed several GID measurements in between XSW scans. This is done in such order to analyze the dynamics of the Ce distribution during the structural change in collapse mode 2. The GID pattern collected between 3 and 5 hours after compression is shown in Fig. 6(c) and between 22 and 24 hours is shown in Fig. 6(d).

As in all other measurements, the monolayer initially formed into a structure with the NN tilt packing mode [see Fig. 6(a)]. However, as the measurements continued, the GID revealed the structural change. Fig. 6(b) shows a rich diffraction pattern, which we assume to be a superposition of two patterns: three lower intensity peaks of PHB located exactly at the same  $Q_{\parallel}$  coordinates (within 1% accuracy) as the PHB peaks in series 2; and two brighter peaks similar to a typical picture of the NN tilt, but with  $Q_{\parallel}$  coordinates different from those in all other series. Also, unlike all other measured NN tilt patterns, the peak above the horizon is to the right of the peak on the horizon. Furthermore, one can see that the bright peak above the horizon is slightly rounded. The roundness of the peaks is clearly observed in the GID pattern in Figs. 6(c), 6(d). Three rounded peaks, again at  $Q_{\parallel}$ , characteristic of the PHB, are seen in Fig. 6(c). No other peaks are in this pattern. This measurement is taken 3.5 and 5 hours after compression of the monolayer. It is noteworthy that the GID pattern measured 24 hours after compression is similar [see Fig. 6(d)], indicating that the monolayer is relatively stable in collapse mode 2. The GID pattern is different in terms of the maximum height of the peaks, but there are still all three PHB peaks and they are also rounded.

## 2.4 X-ray standing waves

We applied X-ray standing wave (XSW) technique to monitor the changes in the location of cerium atoms during the self-assembling reorganization of the AA monolayer. In XSW studies at liquid interfaces, the intensity of secondary radiation (e.g., characteristic fluorescence), excited by the incident X-rays, is measured as a function of the incident angle in the subcritical region  $0 < \theta < \theta_c$ . The angular dependence of fluorescence intensity is known to be highly sensitive to the position of the atoms emitting secondary radiation signal, that allows to locate the atoms by the fitting the corresponding fluorescence curve. For quantitative analysis of XSW data the fluorescence intensity curves are typically simulated using the Parratt equations [25] or optical transfer matrices (see [26, 27] among others).

In our experiments, the intensity of Ce-fluorescence was measured for the solid phase and the two collapse modes (Fig. 7). The XSW measurements for collapse mode 1 were performed at an energy of  $E = 5.8$  keV, the other Ce-fluorescence curves were measured at  $E = 13$  keV.

The XSW measurements for the solid-phase monolayer were carried out 21 hours after the AA monolayer was compressed to  $\pi = 20$  mN/m. Fig. 7(a) shows the angular dependence of integrated intensity for Ce  $L_{\alpha}$  peak obtained in these measurements. From this figure, the intensity of the Ce-fluorescence increases dramatically from zero at  $\theta = 0^{\circ}$  and reaches the sharp maximum near the critical angle  $\theta = \theta_c$ . This is a typical behavior, which is observed for the angular dependence of the fluorescence intensity from atoms distributed in the near-surface region [28]. Theoretical simulations have shown that there is a good agreement between the calculations and the experimental data, for the solid-phase monolayer, which can be obtained within the framework of a two-layer model: the Ce-free top layer (AA monolayer) and the Ce-containing bottom. Both layers were considered to be homogeneous. The theoretical Ce-fluorescence curve in Fig. 7(a) was calculated for the case when Ce atoms are present in a 5 Å thick layer under the top layer with a thickness of 27 Å. Based on these data we can suggest that Ce atoms formed a single layer underneath the AA monolayer, that is a quite reasonable arrangement of Ce atoms for a solid-phase monolayer.

The XSW data for collapse mode 1 are presented in Fig. 7(b). The monolayer was compressed to a surface pressure of  $\pi = 55$  mN/m, after that layer area was held constant. The angular dependence of the Ce-fluorescence intensity was recorded 1.5 hours after the AA monolayer was compressed. As can be seen, this experimental Ce-curve is sharply peaked at the critical angle  $\theta_c$  and is very similar to that recorded for the solid-phase monolayer. This observation is quite remarkable indicating that in the collapse mode 1, Ce atoms are located in the near-surface region.

The arrangement of Ce atoms in collapse mode 2 appeared to be more complicated. XSW data, obtained

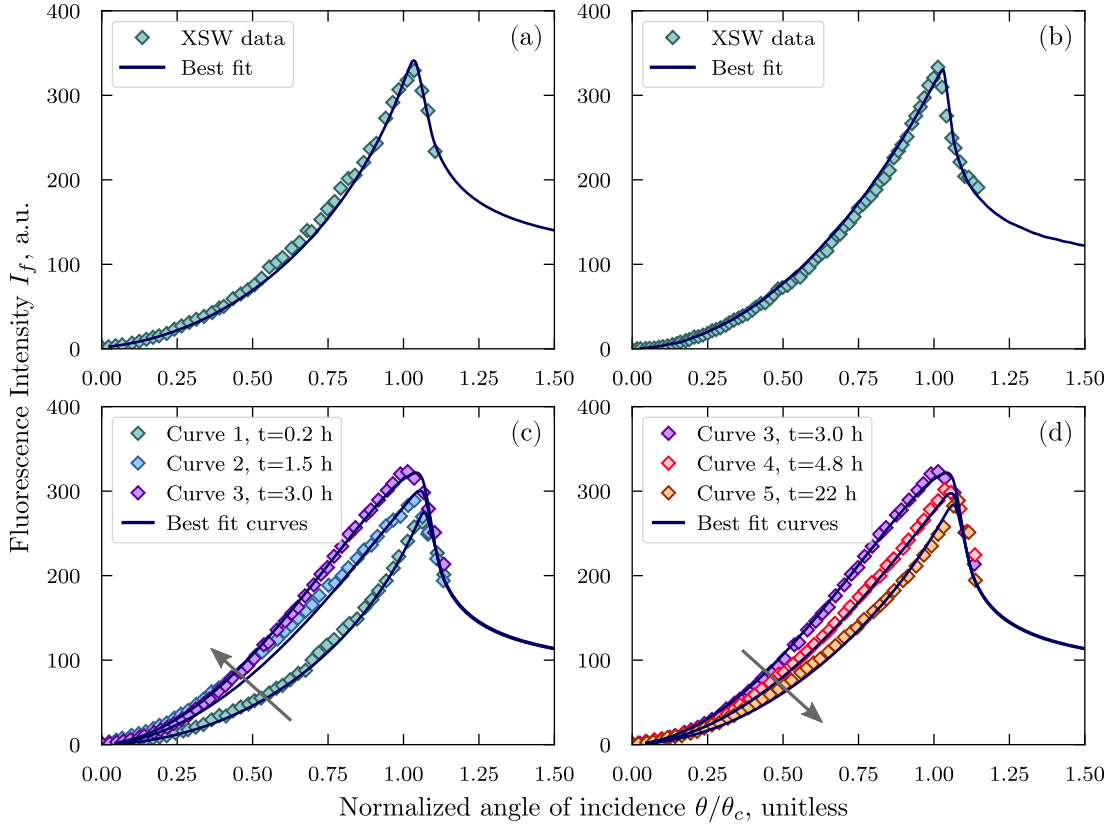


Figure 7: X-ray standing wave measurements: fluorescence intensity characteristic of Ce measured with respect to the angle of incidence  $\theta$ . (a) Measured for the solid phase (one of many typical curves measured in series 1 and 2). (b) Measured for the collapse mode 1 (series 3). (c), (d) The curves measured for the collapse mode 2 (series 4). The curves are measured at different times on the single monolayer. The time elapsed after the monolayer compression is indicated in the legend of the figure. The arrows indicate the direction of change in the slope of the curve over time.

for collapse mode 2, are shown in Figs. 7(c), 7(d). These measurements were taken during GID series 4. A total of six XSW curves were recorded at different times elapsed after compression of monolayer beyond the collapse point ( $\pi > 52$  mN/m). The time of measurement is marked in the legend of Figs. 7(c), 7(d). As can be seen the shape of these curves markedly evolved over time. The first Ce-fluorescence curve exhibited the behavior, which is very similar to that observed for solid-phase monolayer; but the other Ce-fluorescence curves appeared to be significantly different. The most obvious difference is the pronounced convexity near the critical angle. To interpret the observed changes in the Ce-fluorescence curves we hypothesized that some of cerium atoms in collapsed film went upwards. In such a case the experimental Ce-fluorescence can be fitted as the weighted sum of the angular dependencies of the fluorescence intensity from cerium atoms located above the liquid surface and from cerium atoms, which are present underneath the AA monolayer. The shape of the resulting Ce-fluorescence intensity depends mainly on three parameters: two weighting coefficients ( $C_1$  and  $C_2$ ) and the thickness of the Ce distribution above the liquid surface. The best-fit curves in Figs. 7(c), 7(d), were obtained by varying the weight coefficients while keeping the thickness of the Ce distribution above the liquid surface constant at  $55 \text{ \AA}$ . The parameters for the Ce layer located underneath AA film were fixed to those determined from the analysis of the first XSW curve, recorded in this series. Note, that the best-fit parameters for the first XSW curve coincide with the those, obtained for solid-phase AA monolayer.

To understand the general trends in the changes in the location of cerium ions it is convenient to use the weight coefficient ratio  $C_{12} = C_1/C_2$ , that allows to estimate the fractional amount of the cerium ions, located above the liquid surface. The theoretical angular dependencies of the fluorescence intensity in Fig. 7(c), 7(d) were calculated for the following values of this parameter: curve 2:  $C_{12} = 0.1$ , curve 3:  $C_{12} = 0.2$ , curve 4:

$C_{12} = 0.08$  and curve 5:  $C_{12} = 0.03$ . It should be taken into account that good agreement between the theoretical and the experimental curves could be obtained also by varying the thickness of the Ce distribution above the liquid surface. In such a case the changes in the angular dependence of Ce-fluorescence from curve 2 to curve 3 can be explained by the increase of the thickness of the Ce distribution above the liquid surface; whereas the changes in curves 3–5 clearly indicate that this parameter gradually decreases.

Thus, the XSW data obtained for collapse mode 2 provided a clear idea about the Ce-induced processes in the collapsed AA monolayer: In the initial stage (during the first 3 hours), the collapse events are governed by an increase in the thickness of the Ce distribution above the liquid surface and/or an increase in the fraction of Ce atoms located above the liquid surface. In the late stage (during further 19 hours of measurements) the reorganization processes in the AA film are reversed. Namely, the thickness of the Ce distribution above the liquid surface decreases and/or the fractional amount of Ce atoms located above the liquid surface decreases.

### 3 Discussion

Let us now look at all of the above observations from the perspective of the molecular organization of the monolayer. First, note that the arachidic acid monolayer formed on a  $\text{Ce}^{3+}$  solution is thermodynamically very different from the monolayer formed on pure water, as shown by the  $\pi$ - $A$  isotherms in Fig. 1.

The GID data provide information about the structure i.e. translational order of the monolayer. We performed GID measurements on the monolayers with gradually increasing structural complexity. First, we consider the monolayer in the solid phase. Compared to the control series with pure water subphase, the monolayer formed on a subphase with  $\text{Ce}^{3+}$  ions has new structural features. The  $\text{Ce}^{3+}$  ions form an inorganic superstructure underneath the monolayer: a periodically arranged inorganic layer with a  $3 \times 2$  unit cell. This is evidenced by the peaks in range A. These peaks are higher than those of the organic structure, with full width half maximum in the vertical direction  $\delta_z = 0.8 \text{ \AA}^{-1}$ , from which the vertical size of the structure  $d_z \sim 8 \text{ \AA}$  can be estimated to be smaller than that of the arachidic acid hydrocarbon chain  $d_z \sim 22.5 \text{ \AA}$ . The XSW data are insensitive to lateral order, but unlike the GID, they are sensitive to the position of the Ce layer in the vertical direction. The fluorescence intensity curve calculated for the Ce layer underneath the arachidic acid monolayer is in good agreement with the data in Fig. 7(a). This calculation is made for the  $5 \text{ \AA}$  thick Ce layer. This is in agreement with the estimation using the GID. Taken together these, results imply the Ce layer is indeed underneath the organic monolayer, and it does form a laterally periodic inorganic superstructure. This is also consistent with the analysis in [10, 11]. Regarding the chemical composition of the inorganic superstructure, we assume that no nitrate ligands are present in the nearest environment of cerium ions in  $\text{Ce}(\text{NO}_3)_3$  salt solution at the concentration used in our experiments. This assumption is based on the results reported in [29], where X-ray absorption spectroscopy is used to study the interaction of  $\text{Ln}^{3+}$  ions with nitrate ligands in aqueous solutions of  $\text{Ln}(\text{NO}_3)_3$  salts. The formation of an inorganic superstructure has an effect on the structure of the monolayer itself. Compared to the monolayer on a pure water subphase, it is more densely packed with 2% less area occupied by a molecule. This is apparently realized by the NN tilt of the AA hydrocarbon chains.

Another structural feature is revealed in the similarly prepared monolayer formed at the lower temperature  $T = 21^\circ\text{C}$ : the phase mode characterized by the PHB hydrocarbon chains ordering. At higher temperatures, the molecular chains are in the free rotatory state. The hydrocarbon chain have a flattened shape. At lower temperatures, the motion of the molecules is reduced and the shape of the chains begins to play a role. It is then possible to reduce the area occupied by a molecule by aligning the hydrocarbon chains of neighboring molecules. When the azimuth angle between adjacent chains is  $90^\circ$ , it is a herringbone phase mode, and when it is around  $40^\circ$ , it is a PHB. It is illustrative to mention the following. Consider a plot with  $a$  and  $b$  lattice parameters as axes. A point on this plot would represent a monolayer with certain lattice. Also consider the parameters  $(a_\perp, b_\perp)$ , which are the projections of the unit cell onto the plane perpendicular to the molecular chains. In other words, the parameters  $(a_\perp, b_\perp)$  represent the shortest distance between molecules and are therefore more relevant when considering lattice energy calculations. It is described in the literature [5] that monolayers of amphiphilic molecules in the solid phase lie on an arc in this  $(a_\perp, b_\perp)$  plot. Fig. 8 shows the contour plot of the distribution of different studied monolayers, it is based on the data published in [22, 30, 31]. Moreover it is known [22, 32] that the upper left corner of this plot is associated with PHB. In Fig. 8 all the structures considered in our study [see also Table 2] are marked with triangles and their corresponding transverse  $(a_\perp, b_\perp)$  parameters are marked with diamonds. The structures we observed in our study also obey this phenomenological rule: all the diamond markers in Fig. 8 are on this arc. Note that the solid phase monolayer formed at  $T = 21^\circ\text{C}$  is in the upper right corner of this plot. In addition, the PHB phase mode is confirmed by the presence of the



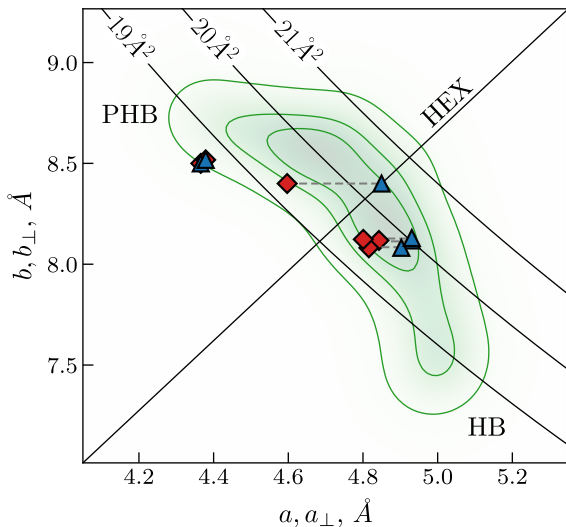


Figure 8: The  $(a, b)$  lattice constants for the monolayers considered in this article. The contour plot shows the arc-shaped distribution of  $(a, b)$  for amphiphilic Langmuir monolayers reported in other studies. This distribution is assumed based on data from [22, 30, 31]. The triangles represent the  $(a, b)$  parameters from the Table 2. The diamonds are the corresponding  $(a_{\perp}, b_{\perp})$  parameters of the same unit cells projected onto the plane perpendicular to the hydrocarbon chains of a fatty acid.

$(2/3\ 0)$  peak in the GID pattern. It should also be noted that the structure of the monolayer has changed. Immediately after compression, the monolayer had a structure similar to that of the monolayer at  $T = 23^{\circ}\text{C}$ . However, with time, a PHB phase mode appeared. The PHB mode coexisted with the NN tilted phase mode. In the PHB, the hydrocarbon chains are not tilted because all corresponding peaks are on the horizon. In Fig. 8 it is shown as follows: the triangular marker corresponding to this structure lies exactly on the diamond, as  $(a, b) \equiv (a_{\perp}, b_{\perp})$ .

Our experimental observations of collapse mode 1 are consistent with previous knowledge of this phase. Namely, once the monolayer is compressed beyond the collapse point, the 2D monolayer begins to reorganize into an ensemble of 3D aggregates on the liquid surface. Indeed, the 3D aggregates are directly visible in the BAM images in Figs. 2(b), 2(c). The implication of this process is that the lateral translational order of the monolayer decays. This is observed in the GID measurements in Fig. 5, where we see a gradual decay of both the GID pattern of the monolayer and the GID pattern of the inorganic superstructure.

It is quite the opposite for the type of structural ordering we refer to as collapse mode 2. The collapse mode 2 was observed at  $T = 21^{\circ}\text{C}$ . First, the BAM images of collapse mode 2 exhibit a mosaic-like structure [see Figs. 2(e), 2(f)]. Second, we were able to observe the GID pattern over all 24 hours of GID measurements that implies that the monolayer retains translational order. This order is maintained over 24 hours of measurements. According to our GID experiments, once the monolayer is beyond the collapse point, it initially retains the NN packing mode, further NN coexists with the PHB, and then only the PHB packing mode remains. See the evolution of the GID pattern in Fig. 6; note that the patterns in Figs. 6(a), 6(b) and in Figs. 6(c), 6(d) are measured on different samples, but all controllable parameters were the same. The PHB packing mode is maintained for an extended period of time once collapse mode 2 is reached. Although the patterns in Figs. 6(c), 6(d) can clearly be attributed to the PHB, since their  $Q_{\parallel}$  coordinates measured at the horizon  $Q_z = 0\ \text{\AA}^{-1}$  match those in series 2 (cf. Fig. 3), the patterns have one unusual feature: the peaks are rounded. We qualitatively associate these roundings with the corrugation of the monolayer. Consider a monolayer with domains that are allowed to lean from being flat on the liquid surface. Unlike the usual GID pattern, which is formed by cylindrical averaging over all possible crystallite positions and thus has a rod-like shape, the GID pattern for the corrugated monolayer is formed not only by this, but also by averaging over all possible orientations of the domains with respect to the surface. Hence the rounding of the peaks. Such peaks must lie on the circle with the origin of the reciprocal space in its center, which is exactly what we observed. However, these peaks are not closed to complete a ring as in 3D powder diffraction. This is because the greater the slope of a domain from the flat position, the less likely that position is in the ensemble.

It is of immediate interest to have a numerical characterization of such a structure. A simple analysis of peak positions and widths provides the orientational and translational structure, and also an estimate of the average size of a single crystal in the 2D powder, if the resolution limit of the experimental setup allows. In most practical cases such an analysis is sufficient. However, when analyzing partially disordered states such as collapse mode 2, more information about the structure is required. This may include the parameters of the

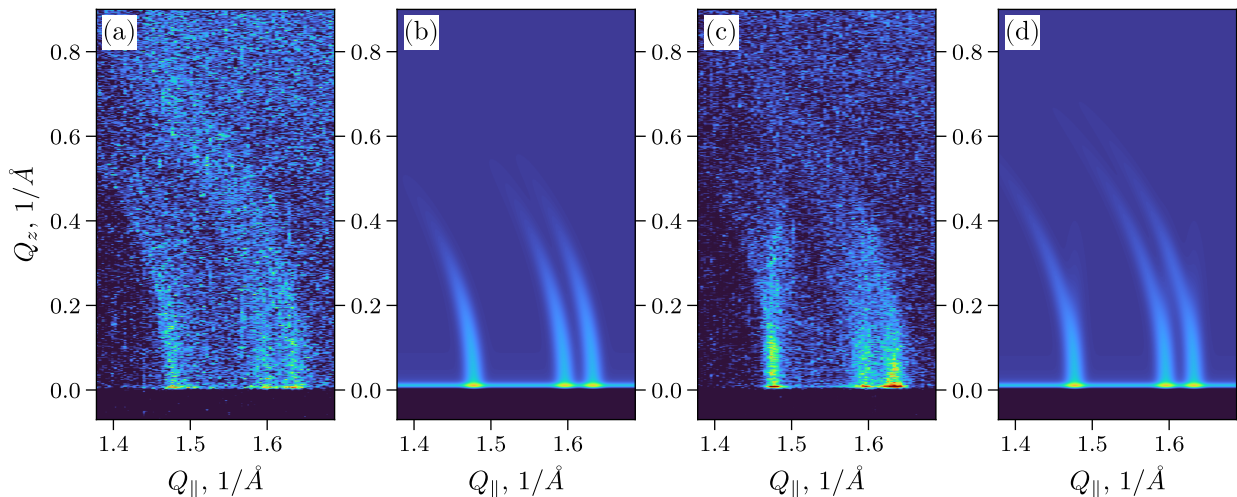


Figure 9: The GID patterns measured in series 4. The start and end times of the measurement in terms of hours elapsed after monolayer compression: (a) 3 –5 hrs. (c) 22 – 24 hrs. [data from the same sample as in Fig. 6] (b,d) Corresponding best-fit GID simulations.

angular distribution of the domains (flat single crystal regions of the corrugated film) or whether the film is partially or fully corrugated. Such an analysis requires numerical simulations based on the physical principles of X-ray diffraction. This approach is much less commonly reported. In this regard, we refer to the works in [33, 34], where the effect of the structure of the fatty acid molecules is carefully considered to calculate line cuts in the 2D GID patterns. In [35], an approach is proposed to calculate the full 2D GID pattern from a polycrystalline monolayer. Two kinds of structural imperfections are taken into account in [35]: thermal vibrations of the molecules leading to Debye-Waller type decay of the diffraction amplitude, and the average size of a single crystal in the monolayer.

We have developed a new approach for physical simulations of the GID. As in [35], it is based on the distorted wave Born approximation. We have derived a mathematical formalism that allows flexibility in the choice of correlation functions, so that different types of structural arrangements can be considered. Namely, it considers the structure with long range and short range translational order. More importantly for this study, it allows the perturbation of the orientational order to be taken into account. In addition, the new approach allows the effect of evanescent wave scattering to be taken into account, which leads to the enhancement of diffuse scattering when the exit angle of the scattered ray is close to  $\theta_c$ . It also allows full 2D pattern simulations. This is again important for our study, since the GID pattern of collapse mode 2 has a complex configuration, i.e. it is difficult to choose a set of points or a set of straight lines in the reciprocal space that fully characterizes this pattern. The report with the underlying mathematical model and the considered physical principles is in preparation [36].

Using the new approach, we performed the simulations of the GID patterns. For the simulations, we assumed that the orientation angle of the domains (the angle between the normal to the surface and the normal to the domain) is normally distributed and that the domains are sufficiently large so that the resulting diffuse scattering is averaged incoherently. We also assumed that there is no preferred azimuthal orientation of the domain, i.e. there is no mosaicity. For simplicity, we also assumed that each domain is a flat single crystal. For the forward simulations we consider the following parameters: average domain size, lattice parameters, tilt angle, effective thickness of the monolayer, standard deviation of the orientation angle  $\sigma_\theta$  and the ratio  $\gamma$  of the corrugated area to the total area of the monolayer. In the context of this research, we focus on the latter two parameters:  $\sigma_\theta$  and  $\gamma$ . The simulations were fit to the experimental data by optimizing the model parameters using the Levenberg-Marquardt algorithm [37]. The resulting best-fit theoretical GID patterns are shown in Fig. 9. First, note that peak rounding is adequately reproduced in the simulations. The simulation in Fig. 9(b) is done for the normally distributed orientation angle, and Fig. 9(d) is a weighted sum between the normally distributed slope of the domain and a simulation for the flat domains. In both the experiment [see Fig. 9(c)] and the simulation [see Fig. 9(d)] one can see the faint straight peak near the brighter rounded one. This is consistent with the observations in XSW where the  $\text{Ce}^{3+}$  ions first upwards above the liquid surface<sup>3</sup> and then the process

was reversed: a part of the monolayer became flat again. The best fit standard deviation of the domain slope distribution for the first GID pattern [see Fig. 9(b)] is  $\sigma_\theta = 6.6^\circ$ . For the second pattern [in Fig. 9(d)] is  $\sigma_\theta = 8.6^\circ$ . The best fit for the latter considers a mixture of  $\gamma = 37\%$  flat domains and the rest being normally distributed. This observation is also in qualitative agreement with the BAM measurements.

## 4 Conclusions

We investigated the effect of aqueous  $\text{Ce}^{3+}$  ions on the structural reorganization of arachidic acid monolayers at different temperatures and surface pressures. The morphology of the monolayer was observed by BAM. The structures were deduced from synchrotron measurements: the lateral ordering was studied with the GID and the vertical distribution of Ce ions with the XSW. By varying the surface pressure and temperature, we observed the structural reorganization of the system. In these observations we reproduced a number of known Ce-induced effects on fatty acid self-assembly. First, the binding of the metal to the carboxylic acid groups leads to the formation of a rigid monolayer with higher crystallinity and reduced molecular area, and such solid-phase monolayers are formed during compression by bypassing the liquid phase, as evidenced by the  $\pi$ - $A$  isotherm measurements.

Second, by interacting with the carboxylic acid groups, the Ce ions may form a laterally ordered layer underneath the organic monolayer. In the GID measurements we observed an inorganic superstructure of Ce ions which is commensurate with the fatty acid monolayer having a  $3 \times 2$  unit cell. The localization of this Ce layer underneath the fatty acid monolayer is confirmed by the XSW measurements. The formation of such an inorganic Ce superstructure can be reproducibly observed at  $T = 23^\circ\text{C}$ .

The third Ce-induced effect was observed in the solid-phase monolayers formed at a lower temperature:  $T = 21^\circ\text{C}$ . Initially, the system behaves like a solid phase at  $T = 23^\circ\text{C}$ . However, with time, another superstructure appears: an organic superstructure. This superstructure does not consist of Ce ions. Instead, it is formed by the molecules of a fatty acid itself. At lower temperatures, the energy stored in the rotational motion of the molecules is reduced, allowing the mutual orientation of adjacent aliphatic chains, which in turn allows the molecular area to be further reduced, forming an even denser monolayer. When the angle between the aliphatic chains of adjacent molecules is about  $40^\circ$ , such a configuration is called PHB. This is an organic superstructure with  $3 \times 1$  cells. Consequently, this breaks the symmetry in the structure factor and an additional peak appears in the GID pattern, which we actually observed. Furthermore, the crystal structure we deduced from the GID pattern corresponds to the PHB phase mode according to the literature.

Finally, we observed a new collapse mode of AA monolayers. Surprisingly, in this collapse mode the monolayer maintains its translational order despite being compressed beyond the collapse point. Instead, the collapse is manifested by the distortion of the long-range orientational order. This is hinted at in BAM images, where a mosaic-like morphology of the film can be seen in the new collapse mode. This is confirmed by GID. Interpretation of the GID data leads to the following conclusions. The monolayer in the new collapse mode consists of 2D crystalline domains that are inclined from the horizontal position. The crystalline structure of a domain corresponds to the PHB packing mode. The domains are inclined according to a normal distribution. We deduced this by fitting forward simulations based on the DWBA to the GID data. Unlike the other collapse modes, the GID pattern did not decay with time. The only change in GID we observed can be attributed to a change in the distribution of domain inclination, the translational order, i.e. crystalline structure of the domains themselves, remained unchanged. By comparing AA monolayers in solid phase and in collapse, we can assume that the packing mode of a solid phase can influence which collapse scenario is realized. Namely, PHB seems to lead to collapse mode 2. Speculatively, the PHB, being a tighter packing than the free-rotating state of the AA monolayer, may explain that the translational order is unchanged in collapse. This is a subject for further study. With this article, we hope to expand the knowledge of the structural reorganization of fatty acids, which may be important for the functionalization of nanomaterials.

## Materials and methods

*Formation of phospholipid monolayer on liquid surface* Nitrate salt  $\text{Ce}(\text{NO}_3)_3 \cdot 6\text{H}_2\text{O}$  (99.99%) was purchased from LANHIT Ltd and used as received. Arachidic acid was purchased from Sigma. To form a lipid monolayer, a solution of arachidic acid in chloroform (concentration of 0.59 mg/ml) was spread on the surface of  $\text{Ce}(\text{NO}_3)_3 \cdot 6\text{H}_2\text{O}$  aqueous solution at a solution pH of  $\sim 5.5$ . The solvent was allowed to evaporate for 15 minutes. The layer was then compressed in a Langmuir trough to the desired surface pressure. All solutions were

prepared using ultrapure water Milli-Q Advantage A10 Water Purification System, (Millipore).

*Surface pressure-area measurements* The Langmuir films were studied on a Minitrough Extended Langmuir trough (KSV) with a maximum interfacial area of 558 cm<sup>2</sup>. The compression rate was 3.75 cm<sup>2</sup>/min. External vibrations of the Langmuir trough were damped by an active vibration damper (Accurion).

*Brewster Angle Microscopy* BAM images were obtained using a Brewster angle microscope (model BAM-300, KSV NIMA) coupled to a temperature-controlled Langmuir trough. A polarized He-Ne laser (wavelength 632.8 nm) was used as the light source, with the beam directed at the air/water interface at an angle of 53.1° (the Brewster angle for water). The reflected beam was collected with a 10× objective; images were taken with a USB camera and corrected with a KSV NIMA software package. Measurements were performed at 21°C and 23°C.

*Synchrotron measurements* GID and XSW studies were performed at the bending magnet beamline LANGMUIR (Kurchatov Center for Synchrotron Radiation, Moscow, Russia), which is equipped with a customized Langmuir trough. The closed Langmuir trough was flushed with water vapor saturated helium to reduce the scattering of the incident X-rays and to reduce the evaporation of the liquid subphase, thus keeping the liquid surface position fixed. The photon energy of the incident beam for all GID measurements was 13 keV. GID measurements were performed at  $\theta = 0.8\theta_c$  ( $\theta_c$  is the critical angle of total external reflection for water). The diffracted intensity in the  $Q_z$  direction was recorded using a linear position sensitive detector (Mythen) with a vertical stripe size of  $\mu\text{m}$ . For XSW measurements, the fluorescence signal was recorded by an energy dispersive Vortex EX detector mounted perpendicular to the liquid surface. The characteristic fluorescence spectra were recorded for each angle of incidence in the angular range corresponding to the total external reflection region.

## Funding information

This research was funded by the Ministry of Science and Higher Education of the Russian Federation (grant no. FSFZ-2024-0003).

## Acknowledgments

The authors are deeply indebted to Dr. Vladimir Kaganer and Dr. Boris Ostrovskii for fruitful discussions, insightful advice, and helpfulness.

## References

- [1] C. M. dos Santos, A. J. Harte, S. J. Quinn, and T. Gunnlaugsson, "Recent developments in the field of supramolecular lanthanide luminescent sensors and self-assemblies," *Coordination Chemistry Reviews*, vol. 252, no. 23, pp. 2512–2527, 2008. 17th International Symposium on the Photochemistry and Photo-physics of Coordination Compounds.
- [2] D. J. Wales and J. A. Kitchen, "Surface-based molecular self-assembly: Langmuir-Blodgett films of amphiphilic Ln(III) complexes," *Chemistry Central Journal*, vol. 10, p. 72, Nov 2016.
- [3] K. Ariga, Y. Yamauchi, T. Mori, and J. P. Hill, "25th anniversary article: What can be done with the Langmuir-Blodgett method? Recent developments and its critical role in materials science," *Advanced Materials*, vol. 25, no. 45, pp. 6477–6512, 2013.
- [4] L. Bosio, J. Benattar, and F. Rieutord, "X-ray reflectivity of a langmuir monolayer on water," *Revue de Physique Appliquée*, vol. 22, no. 8, p. 775–778, 1987.
- [5] V. M. Kaganer, H. Möhwald, and P. Dutta, "Structure and phase transitions in langmuir monolayers," *Rev. Mod. Phys.*, vol. 71, pp. 779–819, Apr 1999.
- [6] D. E. Barry, J. A. Kitchen, L. Mercs, R. D. Peacock, M. Albrecht, and T. Gunnlaugsson, "Chiral luminescent lanthanide complexes possessing strong (samarium, SmIII) circularly polarised luminescence (CPL), and their self-assembly into Langmuir–Blodgett films," *Dalton Trans.*, vol. 48, pp. 11317–11325, 2019.

- [7] J. Kmetko, A. Datta, G. Evmenenko, and P. Dutta, “The effects of divalent ions on langmuir monolayer and subphase structure: a grazing-incidence diffraction and bragg rod study,” *The Journal of Physical Chemistry B*, vol. 105, pp. 10818–10825, Nov 2001.
- [8] F. Leveiller, D. Jacquemain, M. Lahav, L. Leiserowitz, M. Deutsch, K. Kjaer, and J. Als-Nielsen, “Crystallinity of the double layer of cadmium arachidate films at the water surface,” *Science*, vol. 252, no. 5012, pp. 1532–1536, 1991.
- [9] V. Dupres, S. Cantin, F. Benhabib, F. Perrot, P. Fontaine, M. Goldmann, J. Daillant, and O. Konovalov, “Superlattice formation in fatty acid monolayers on a divalent ion subphase: Role of chain length, temperature, and subphase concentration,” *Langmuir*, vol. 19, pp. 10808–10815, Dec 2003.
- [10] M. Miller, M. Chu, B. Lin, M. Meron, and P. Dutta, “Observation of ordered structures in counterion layers near wet charged surfaces: A potential mechanism for charge inversion,” *Langmuir*, vol. 32, pp. 73–77, Jan 2016.
- [11] M. Miller, M. Chu, B. Lin, W. Bu, and P. Dutta, “Atomic number dependent “structural transitions” in ordered lanthanide monolayers: Role of the hydration shell,” *Langmuir*, vol. 33, pp. 1412–1418, Feb 2017.
- [12] P. Zhang, T. Pham, X. Zheng, C. Liu, P. L. Plata, P. Král, W. Bu, B. Lin, and Y. Liu, “Spontaneous collapse of palmitic acid films on an alkaline buffer containing calcium ions,” *Colloids and Surfaces B: Biointerfaces*, vol. 193, p. 111100, 2020.
- [13] D. Vaknin, W. Bu, S. K. Satija, and A. Travasset, “Ordering by collapse: formation of bilayer and trilayer crystals by folding langmuir monolayers,” *Langmuir*, vol. 23, pp. 1888–1897, Feb 2007.
- [14] C. D. Lorenz and A. Travasset, “Atomistic simulations of langmuir monolayer collapse,” *Langmuir*, vol. 22, pp. 10016–10024, Nov 2006.
- [15] S. Nayak, R. R. Kumal, and A. Uysal, “Spontaneous and ion-specific formation of inverted bilayers at air/aqueous interface,” *Langmuir*, vol. 38, no. 18, pp. 5617–5625, 2022. PMID: 35482964.
- [16] A. Sthoer, E. M. Adams, S. Sengupta, R. W. Corkery, H. C. Allen, and E. C. Tyrode, “La<sup>3+</sup> and Y<sup>3+</sup> interactions with the carboxylic acid moiety at the liquid/vapor interface: Identification of binding complexes, charge reversal, and detection limits,” *Journal of Colloid and Interface Science*, vol. 608, pp. 2169–2180, 2022.
- [17] B. A. Capistran and G. J. Blanchard, “Effects of Cu(II) on the formation and orientation of an arachidic acid Langmuir–Blodgett film,” *Langmuir*, vol. 35, pp. 3346–3353, Mar 2019.
- [18] R. Johann, G. Brezesinski, D. Vollhardt, and H. Möhwald, “The effect of headgroup interactions on structure and morphology of arachidic acid monolayers,” *The Journal of Physical Chemistry B*, vol. 105, pp. 2957–2965, Apr 2001.
- [19] E. Hatta and J. Nagao, “Topological manifestations of surface-roughening collapse in langmuir monolayers,” *Phys. Rev. E*, vol. 67, p. 041604, Apr 2003.
- [20] J. Strzalka, E. DiMasi, I. Kuzmenko, T. Gog, and J. K. Blasie, “Resonant x-ray reflectivity from a bromine-labeled fatty acid langmuir monolayer,” *Phys. Rev. E*, vol. 70, p. 051603, Nov 2004.
- [21] V. Dupres, S. Cantin, F. Perrot, P. Fontaine, and M. Goldmann, “Evidence of a tilted and herringbone structure in cadmium behenate Langmuir–Blodgett ultrathin films: Comparison with Langmuir monolayers,” *The Journal of Chemical Physics*, vol. 116, pp. 3822–3827, 03 2002.
- [22] I. Kuzmenko, V. M. Kaganer, and L. Leiserowitz, “Packing of hydrocarbon chains and symmetry of condensed phases in langmuir monolayers,” *Langmuir*, vol. 14, pp. 3882–3888, Jul 1998.
- [23] C. Fradin, J. Daillant, A. Braslau, D. Luzet, M. Alba, and M. Goldmann, “Microscopic measurement of the linear compressibilities of two-dimensional fatty acid mesophases,” *The European Physical Journal B - Condensed Matter and Complex Systems*, vol. 1, pp. 57–69, Jan 1998.

- [24] J. B. Peng, G. T. Barnes, I. R. Gentle, and G. J. Foran, "Superstructures and correlated metal ion layers in langmuir-blodgett films of cadmium soaps observed with grazing incidence x-ray diffraction," *The Journal of Physical Chemistry B*, vol. 104, pp. 5553–5556, Jun 2000.
- [25] L. G. Parratt, "Surface studies of solids by total reflection of x-rays," *Phys. Rev.*, vol. 95, pp. 359–369, Jul 1954.
- [26] A. Gibaud and S. Hazra, "X-ray reflectivity and diffuse scattering," *Current Science*, vol. 78, pp. 1467–1477, 2024/11/18/ 2000. Full publication date: 25 June 2000.
- [27] K. V. Nikolaev, A. I. Safonov, O. A. Kondratev, G. V. Prutskov, I. A. Likhachev, I. A. Subbotin, M. M. Borisov, S. A. Tikhomirov, E. M. Pashaev, and S. N. Yakunin, "Grazing-emission X-ray fluorescence as a multiprobe tool for thin-film metrology," *Journal of Applied Crystallography*, vol. 56, pp. 1435–1445, Oct 2023.
- [28] S. I. Zheludeva, N. N. Novikova, M. V. Kovalchuk, N. D. Stepina, E. A. Yurieva, E. Y. TereschenKO, and O. V. Konovalov, *Biomembrane models and organic monolayers on liquid and solid surfaces*, pp. 355–368. World Sci. Publ., 2013.
- [29] T. Yaita, H. Narita, S. Suzuki, S. Tachimori, H. Motohashi, and H. Shiwaku, "Structural study of lanthanides(III) in aqueous nitrate and chloride solutions by exafs," *Journal of Radioanalytical and Nuclear Chemistry*, vol. 239, pp. 371–375, Feb 1999.
- [30] F. Bringezu, B. Dobner, and G. Brezesinski, "Generic phase behavior of branched-chain phospholipid monolayers," *Chemistry*, vol. 8, pp. 3203–3210, July 2002.
- [31] F. Bringezu, G. Brezesinski, and H. Möhwald, "Influence of side-chain length on phospholipid ordering in two dimensions," *Chemistry and Physics of Lipids*, vol. 94, no. 2, pp. 251–260, 1998.
- [32] C. Buzano, A. Pelizzola, and M. Pretti, "Herringbone ordering and lattice distortions in a planar-molecule model for langmuir monolayers," *Phys. Rev. E*, vol. 62, pp. 5230–5241, Oct 2000.
- [33] J. Pignat, J. Daillant, L. Leiserowitz, and F. Perrot, "Grazing incidence x-ray diffraction on langmuir films: toward atomic resolution," *The Journal of Physical Chemistry B*, vol. 110, pp. 22178–22184, Nov 2006.
- [34] J. Pignat, J. Daillant, S. Cantin, F. Perrot, and O. Konovalov, "Grazing incidence x-ray diffraction study of the tilted phases of langmuir films: Determination of molecular conformations using simulated annealing," *Thin Solid Films*, vol. 515, no. 14, pp. 5691–5695, 2007. The Ninth International Conference on Surface X-Ray and Neutron Scattering.
- [35] M. A. Chuev, G. V. Prutskov, N. N. Novikova, E. M. Pashaev, O. V. Konovalov, N. D. Stepina, A. V. Rogachev, and S. N. Yakunin, "Theoretical approach to analysis of x-ray grazing-incidence diffraction from 2d crystals," *Crystallography Reports*, vol. 65, pp. 772–778, Sep 2020.
- [36] L. R. Muftakhova, K. V. Nikolaev, N. N. Novikova, A. V. Rogachev, B. I. Ostrovsky, and S. N. Yakunin, "X-ray diffraction in langmuir monolayers with disturbed orientation order," *Crystallography Reports*, forthcoming.
- [37] J. J. Moré, "The levenberg-marquardt algorithm: Implementation and theory," in *Numerical Analysis* (G. A. Watson, ed.), (Berlin, Heidelberg), pp. 105–116, Springer Berlin Heidelberg, 1978.